Materials Physics and Mechanics 48 (2022) 69-90
Research article

Received: August 24, 2021
Accepted: November 24, 2021

MICROSTRUCTURE CHARACTERIZATION OF WELD CONSUMABLE CONDITION ON RESIDUAL STRESS, FLEXURAL STRENGTH, AND ROOM TEMPERATURE TENSILE TESTS OF P92 STEEL

Vinay Kumar Pal✉, L.P. Singh

Department of Mechanical Engineering, Sam Higginbottom University of Agriculture, Technology And Sciences Allahabad, 211007, U.P, India

✉ gaurishankar.vinaypal@gmail.com

Abstract. The present manuscript describes the flexural strength, lower critical stress, and tensile stress of P92 steel welds was determined with respect to different conditions. The residual stresses axial and transverse stress were also measured blind hole drilling methods for the different conditions of welding consumables. The peak value of residual stresses was measured at the centre of the fusion zone. The maximum value of transverse stress was measured to be 355 MPa for case IV in which electrode after baking dipped in 20W oil for 10 minutes. The experimentally determined residual stresses correlated well with the numerically estimated residual stress. The microstructure characterization after PWHT and N&T treatment. For microstructure study, optical microscope and scanning electron microscope have been utilized. To characterize the mechanical behavior, tensile test for multi-pass welds joint, hardness and Charpy impact toughness and fracture surface morphology test, flexural test for multi-pass welds joint were performed.
Keywords: P92 steel, microstructure, mechanical properties, tensile properties, PWHT

Acknowledgements*. No external funding was received for this study.*

Citation: Pal V.K., Singh L.P. Microstructure characterization of weld consumable condition on residual stress, flexural strength, and room temperature tensile tests of P92 steel // Materials Physics and Mechanics. 2022, V. 48. N. 1. P. 69-90. DOI: 10.18149/MPM.4812022_7.

1. Introduction

Joining of the structural component, piping, and pressure vessels used in nuclear, thermal fertilizer, and chemical power industries are generally carried out by the welding process that results in residual stress, shrinkage stress, and distortion at a markable level. In the welding process, localized heating and cooling lead to the formation of complex residual stress and distortion that results in catastrophic failure of the welded joint. Localized heating and cooling of the base, solidification shrinkage of the weld, internal constraint, an external constraint like tacking, and phase transformation result in the formation of residual stresses and distortion [1–3]. Differential contraction of the weld and adjacent base metal causes thermal straining that leads to distortion and shrinkage stress in welded structure [4,5].

Thermal straining along the welding direction results in the formation of longitudinal

http://dx.doi.org/10.18149/MPM.4812022_7

shrinkage while the strain perpendicular to the direction of welding cause the transverse shrinkage [6]. The welding distortion occurs due to the internal forces developed in the structure from the resulting combined stresses. Distortion is treated as the pattern of permanent strains that remain in the structure after the completion of the welding process. In the arc welding process, the material is subjected to a temperature more than the melting temperature of the metal. The welding cycle is elevated to rapid heating and cooling. Compared to the weld structure, the size of the weld pool is very small and expansion and contraction of the weld are prevented by the adjacent base metal. During the heating cycle, expansion of the heated zone leads to the formation of compressive residual stress, and the cooling cycle results in shrinkage which is prevented by the base metal. After the cooling, shrinkage resistance causes the formation of tensile residual stress in the weld zone which is balanced with the compressive residual stress of base metal [3]. Distortion and residual stress cannot be removed completely but they can be minimized. Excessive constraint during the welding process leads to the formation of high residual stress while low residual stress formed during the free expansion and contraction. During the welding process, parent metal will either resist the distortion or shrinkage resulting in residual stress, or it follows the shrinking movement of the weld pool resulting in distortion and shrinkage [7]. The residual stress and distortion are influenced by many parameters like the welding process, welding parameters, number of processes, groove geometry, material properties, and phase transformation. Weld-induced tensile residual stress in welded components leads to the HIC, buckling deformation, stress corrosion cracking (SCC), reduction in fatigue life, and brittle fracture [8–10]. The solid phase transformation and welding boundary condition play a crucial role in final stress distribution. Solid-phase transformation occurs in two different manners. The first one is the formation of secondary phase particles during the heating process and the second one is the transformation of the matrix from one atomic packing to the other during the heating and cooling process. The transformation that occurs during the heating and cooling cycle influence the formation of residual stress level. The character of the material is mainly responsible for phase transformation. In P91 steel, the martensitic transformation occurs during the welding cycle whose effect is more complex and acts to influence the level of stress in the transformed zone. Cottam et al. [2] studied the effect of both types of phase transformation on stress formation. They had reported that the martensitic transformation is more complex and helps to reduce the magnitude of residual stress in the transformed zone. The point at which martensitic transformation starts resulted in an increase in stress level in the adjacent non-deformed zone. In P91 steel weldment, cooling cycle leads the transformation of austenite to martensite. During the transformation from austenite, the stress level was observed to be decreased up to Ms temperature and after that increased to final martensitic transformation. The austenite to martensite transformation resulted in the formation of compressive stresses. The tensile residual stress was reduced with an increase in volume fraction of martensite by controlling the heat input and cooling rate. Austenitizing of steel results in structure transformation from BCC (ferrite) to FCC (austenite) that leads to a reduction in volume. During the cooling process, the transformation of austenite to martensite results in BCT structure formation that leads to increased volume, [11].

Dong et al. [12] studied the effect of pipe wall thickness on residual stress distribution. Pipe wall thickness showed a strong influence on residual stress specifically on the axial component of residual stress. Axial residual stress showed compressive nature at the outer surface while tensile at the inner surface near the vicinity of the weld. The axisymmetric model was also developed for the numerical prediction of residual stress. In start and stop points of welding, the presence of both high magnitude tensile and compressive resulted in stress gradient. Yaghi et al. [11] studied the residual stress distribution in the P92 welded pipe

by incorporating the solid phase transformation. It was observed that the solid-state phase transformation (SSPT) in P92 welding has a great influence on residual stress distributions and their magnitude. Zubairuddin et al. [13] also reported the martensitic phase transformation effect on residual stress distribution and observed almost similar results. SSPT during welding resulted in considerable lowering in the magnitude of axial and hoop stress on the outer surface of the welded pipe (HAZ) and half of the weld fusion zone. Den and Hidekazu [14] had reported that martensitic transformation not only reduced the magnitude of residual stress but also altered the sign of residual stress. The FE simulation showed a good agreement with experimental results when the martensitic transformation was taken into account. Murakawa et al. [15] continued the same research and studied the effect of Ms temperature on the magnitude of tensile residual stress developed in the weld zone. A low Ms temperature helped to develop a compressive stress component that reduced the magnitude of net tensile residual stress within the fusion zone. The magnitude of compressive stress was observed to be increased with the decrease in the Ms-temperature and became saturate at a temperature of about 200^{o}C. The tensile nature of longitudinal stress developed in the heat-affected zone was observed to be unaffected by the M_s-temperature. Preheating has also observed a great influence on the magnitude of residual stress and its distribution. Preheating before the welding caused a considerable lowering of peak temperature and cooling rate. Zubairuddin et al. [13] reported that preheating resulted in are duction in peak tensile residual stress and distortion. Finite element (FE) modeling is most commonly used for numerical analysis [16,17]. A lot of work has been performed related to the study of the effect of the welding process, groove geometry, welding parameters, PWHT, and a number of welding passes on shrinkage and shrinkage stress in pipe and plate weldments [18,19]. Ghosh et al. [6] performed an analytical study on shrinkage stress mode, magnitude, and distribution in different quadrants of GMAW and pulse GMAW welded pipe for different weld groove designs. The mode and magnitude of shrinkage stress in a different quadrant were observed to be non-uniform and varied as a function of the welding process, parameters, and groove geometry. Pulse GMAW process was resulted in lower magnitude and uniform distribution of transverse shrinkage stress compared to GMAW. Higher heat input during the welding process resulted in a higher magnitude of transverse shrinkage stress. For constant heat input, narrow groove design produced the lower shrinkage stress compared to conventional groove design. The multi-pass welding, the weld metal is subjected to localized solidification shrinkage [20]. The repetitive influence of the thermal cycle from subsequent weld passes affects the development of stress in weld grooves up to a certain extent, and finally, it causes a continuous change in groove design and groove area with every weld passes [12]. The change in groove size with subsequent pass results in groove angle variation and it will not be uniform at all locations in each quadrant of the pipe. The change in groove size and groove area was observed to be more in the case of V-groove weld design than narrow groove and this occurred due to less weld metal deposition in a narrow groove. Sattari-Far and Javadi [21] studied the welding sequence effect on distortion in pipe-pipe butt joints. The experimental results were validated with numerically obtained values. Welding leads to the diametrical variation in the pipe that mainly depends on the welding sequence. The diametrical variation in the welding section was observed to be decreased (negative) and became zero at some distance away from the welding section and afterward increased. Deng et al. [20] performed the residual stress estimation in the multi-pass butt-welded thick pipe by strain gauge method and the experimentally observed residual stress value matched with numerically obtained residual stress value from 2-D axisymmetric FE model. The influence of weld metal yield strength on residual stress was also observed. The stresses induced in the material during the strengthening and heat treatment process have observed a great effect on residual stresses.

The strengthening of material resulted in a significant increase in material yield strength and this might be the cause of higher residual stress after welding.

Kim et al. [22] predicted the residual stress distribution in P92 welded structure by using the neutron diffraction technique and to enhance the quality of results, the experimental results were fairly matched with the numerical results obtained from FE simulation. Welding sequence has a great influence on residual deformation. Ghosh et al. [23] studied the effect of Pulse GMAW and GMAW process on transverse shrinkage stress and distortion of the thick butt-welded plate. It was observed that the use of pulse GMAW produced low shrinkage stress, bending stress, and distortion compared to GMAW process. For a given heat input, narrow groove weld design produced lower stresses and distortion compared to V groove design but the too much narrow groove resulted in higher bending stress. For narrow groove weld design with pulse GMAW, about 35-45% reduction in transverse shrinkage was reported compared to conventional V groove pulse GMAW and SMAW [24]. Arunkumar et al. [25] reported that GTAW process minimized the transverse shrinkage by about 30% compared to GMAW process due to lower heat input application in GTAW. Basavaraju performed a simplified elastic-plastic approach to measure the strains' formation due to radical shrinkage of pipe butt weld [7]. A number of works have also been reported related to 3D finite element (FE) simulation of residual stress and distortion. Yaghi et al. [26] performed a comparative study of numerically and experimentally evaluated residual stress value for P91 pipe weldments and showed good agreement between the results. The residual stresses at the outer surface were measured using X-ray diffraction while inner surface residual stress measurement was performed using the deep-hole drilling technique. Paddea et al. [27] performed an experimental study to measure the residual stress distribution in P91 girth pipe weldment and also study the effect of PWHT on their magnitude and distribution. The boundary of HAZ and base metal (IC-HAZ) showed the maximum tensile residual stress value of about 600 MPa. The maximum tensile hydrostatic stress (400 MPa) was also observed near the vicinity of HAZ. The PWHT resulted in considerable lowering in residual tensile stress (about 24% of yield strength of base metal) and hydrostatic stress (50 MPa). The compressive residual stress was reported in weld fusion zone near the final weld pass. Venkata et al. [28] studied the effect of PWHT on residual distribution in electron beam welded P92 plate. The residual stress was measured using neutron diffraction technique and compared with numerically predicted values. To minimize the residual stress, maximum PWHT duration about 2 hours and temperature about 770 ^{o}C below than Ac_1 temperature was reported. Chuvas et al.[29] also reported that PWHT at 760°C for 2 h resulted in a drastic decrease in residual stress value both in root and cap of the weld. Kulkarni et al. [30] had performed a comparative analysis of SMAW, GMAW, and pulse GMAW processes and their effect on residual stress formation during welding of thick stainless steel pipe. The pulse GMAW process produced relatively lower residual stress at the top and root of the weld. Zhao et al. [31] also reported the high magnitude of residual stress near the start/stop position for dissimilar multi-pass welding of 12Cr1MoV/P92 pipe. Hempal et al. [32] performed the residual stress measurement in multi-pass welded ferritic-pearlitic pipes, using the X-ray diffraction technique. In weld zone, phase transformation has observed a minor influence but in HAZ a great influence was observed due to the formation of high strength martensitic phase. At the inner surface of weld toe, maximum tensile axial residual stress was observed which is considered as preferential sites for the fatigue crack initiation. The work in the field of modeling of manufacturing processes such as electric discharge grinding process and high speed selective jet electrodeposition process as well as the residual stress estimation and their minimization in ultrasonic assisted turning of 4340 hardened steel has also been reported in literature [33-35].

The aim of the present investigation is to various welding process parameter specimen

thickness. The P92 steel plate joints were prepared using the shielded metal arc welding processes for four different conditions for weld consumables and flexural strength of P92 steel weldments were studied. The residual stresses were calculated by the blind hole drilling method.

2. Experimental detail

Material and weld consumable. The chemical composition of P92 steel in the 'as-received' state as given in Table 1 was analyzed using an optical emission spectrometer. The low hydrogen welding consumable was used to make the weld joints by using the shielded metal arc welding (SMAW) process. The 9CrMoV-N (E9015-B9) electrode was selected for SMAW having chemical composition is given in Table 1.

Table 1. Chemical composition of the cast and forged (C&F) P92 steel, %wt

Element	Chemical composition, wt%											
	C	Mn	S	Si	Cr	Mo	V	N	Ni	Cu	Nb	Ti
P92 steel	0.11	0.54	0.01	0.27	8.49	0.95	0.22	<0.02	0.35	0.06	0.06	0.012
electrode	0.10	0.55	0.008	0.25	9.0	1.0	0.20	-	0.3	0.05	0.04	-

The microstructure of C&F P92 steel is shown in Fig. 1(a) and (b), respectively. It consisted of mainly elongated martensitic lath with an average width of 0.782±0.238 µm. It also consisted of several elements such as lath blocks, lath packets, carbide, and carbonitrides precipitates. The microstructure is mainly composed of tempered lath martensite. The fine precipitates inside the lath blocks are confirmed as V and Nb-rich MX type precipitates with size in the range of 20-40 nm [36]. The lath boundaries are decorated with precipitates of $M_{23}C_6$ carbides in form of different morphology and sizes ranging from 69 nm to 272 nm, as shown in Fig. 1(b). The average size of precipitates at the lath boundaries and in the matrix was calculated to be 151 ± 46 nm. The lath directions are clearly indicated by the yellow dotted lines in micrographs, as shown in Fig. 1(a-b). The mechanical properties of C&F P92 steel are given in Table 2.

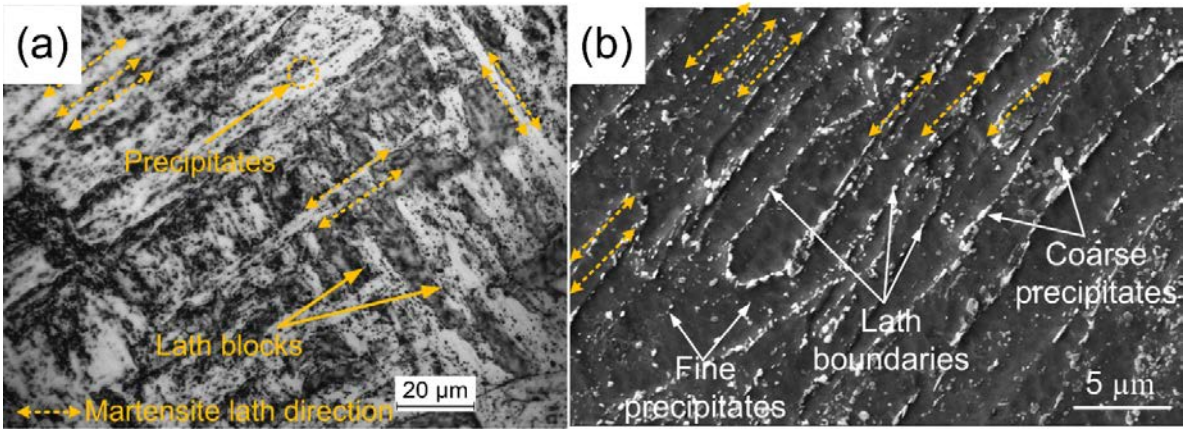

Fig. 1. (a) Optical micrograph of as-received cast and forged P92 steel and (b) SEM micrograph of P92 steel

Table 2. Mechanical properties of C&F P92 steel in as-received state

Grade 92 steel	Yield strength(MPa)	Tensile strength(MPa)	Elongation (%)	Hardness (HV)	Impact toughness(Joules)
	455±10	655±6.36	22±0.25	231±5.38	96±5

Tensile test. Standard tensile test specimens were prepared according to ASTM A337 with gauge length and width of 100 mm and 15 mm, respectively. The single 100 mm long pass of SMAW bead was deposited over the gauge length. The bead height was 1.65±0.13 mm. The welding was carried out with parameters identical to those used during diffusible hydrogen analysis. After the bead deposition, the tensile specimens were quenched in the ice water immediately and then placed in acetone at -50°C for 10 min. The cryogenic condition was implemented to stop the mobility of hydrogen in the weld metal. The test was carried out as per reference [37]. After the cooling, the sample was loaded on UTM at room temperature for a crosshead speed of 1 mm/min. The schematic of the tensile test specimen is shown in Fig. 2. For multi-pass welding, welding process parameters are listed in Table 3.

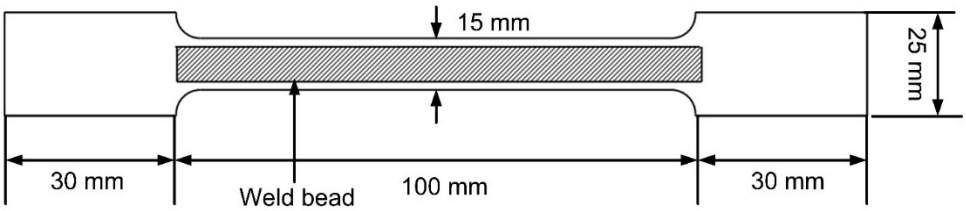

Fig. 2. Schematic of tensile specimen

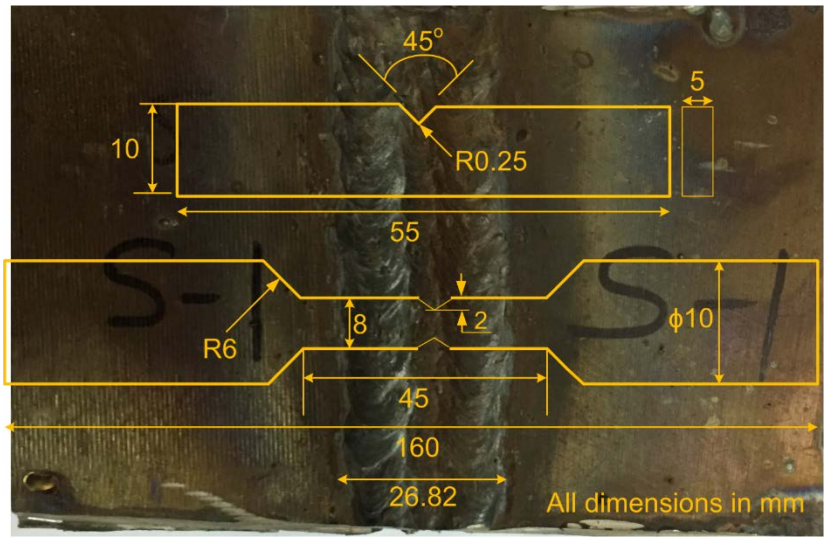

Fig. 3. Schematic of tensile and Charpy toughness specimen machined from the welded plate

3. Result and discussion

As-received material. To compare the effect of weld consumable condition and heat treatment, room temperature tensile tests were performed at the crosshead speed of 1 mm/min. For the tensile test, the round sub-size specimen with a gauge diameter of 8 mm was machined as per ASTM E8-04 standard. In the tensile specimen, the notch of depth 2 mm was prepared at the center of the weld (Fig. 3). To perform the room temperature Charpy toughness test sub-size specimen of dimension 55mm×10mm×5mm were machined (Fig. 3). The notch angle and radius were kept at 45° and 0.25 mm, respectively.

Microstructure in the as-welded condition. Typical secondary electron micrograph of sub-zones of P92 plate weldments in as-welded condition are shown in Fig. 4(a-d). Typical untempered columnar laths are clearly seen in the weld fusion zone, as shown in Fig. 4(a). In the weld fusion zone, complete dissolution of precipitates caused a hard martensitic lath structure. The CGHAZ zone is characterized by PAGBs with no precipitates along the

PAGBs and lath boundaries, as shown in Fig. 4(b). Inside the PAGBs, martensite structures were formed within lath blocks and packets/groups having a spatial orientation in one direction.

Table 3. Welding process parameters for root pass and filler pass

Sample 1	Current (amp)	Voltage (volt)	Time (sec)	Travel speed (mm/sec)	Efficiency (η)	Heat input (kJ/mm)
Root pass 1	115-120	14-16	70	2.14	0.60	0.494
Root pass 2	110-115	12.0-14.0	70	2.14	0.60	0.410
1	140	22.0-23.0	45	3.20	0.80	1.177
2	144	21.6-22.8	44	3.40	0.80	1.195
3	144	22.5-23.6	28	5.36	0.80	1.240
4	144	21.8-23.3	33	4.55	0.80	1.213
5	144	22.8-23	39	3.85	0.80	1.232
6	144	21-22.8	35	4.29	0.80	1.178
7	144	21-23	35	4.29	0.80	1.184
8	144	21.5-23	36	4.17	0.80	1.197
9	144	21.5-23	30	5.00	0.80	1.197
10	144	21-23	31	4.84	0.80	1.184
11	148	23.3-24	40	3.75	0.80	1.308
12	151	22-25.6	30	5.00	0.80	1.343
13	151	22-24.5	30	5.00	0.80	1.312
14	151	21.2-24	29	5.17	0.80	1.275

The columnar laths inside the PAGBs are also formed in the CGHAZ. In the FGHAZ, small austenite grains are formed. The precipitates in FGHAZ dissolve partially because of low transformation temperature. Hence, FGHAZ is characterized by tempered martensite, coarse precipitates, fine precipitates, and fine grains. In FGHAZ, equiaxed laths are formed with the PAGBs, as shown in Fig. 4(c). In P92 pipe weldments, the most common type IV cracking is generally originated from the weak FGHAZ portion. The micrograph of ICHAZ is shown in Fig. 4(d). The ICHAZ is characterized by the partial dissolution of precipitates, coarsening of existing precipitates, and auto-tempering of martensite during the weld heating cycle. The ICHAZ shows a mixed microstructure of newly developed fresh columnar lath and temper equiaxed lath. In ICHAZ, PAGBs and sub-grain boundaries are decorated with coarse $M_{23}C_6$ precipitates while fine Nb and V carbonitride precipitates along the grain boundaries and inside the matrix region.

Microstructure characterization after PWHT and N&T treatment. The microstructure of sub-zones of P92 plate weldments in PWHT and N&T conditions is depicted in Fig. 5(a-h). The weld fusion zone is shown in Fig. 5(a-b). In PWHT condition, the weld fusion zone is characterized by tempered columnar laths, lath boundaries, and precipitates across the laths and inside the matrix region. A large fraction area of precipitates was noticed in the weld fusion zone after the PWHT. The coarse $M_{23}C_6$ precipitates are clearly seen from Fig. 5(a). The distribution of precipitates inside the matrix region and across the boundaries is seen in the higher magnification micrograph (Fig. 5-top right portion). After the N&T treatment, the columnar laths become disappear. Coarse PAGBs and tempered equiaxed laths are noticed after the N&T treatment, as shown in Fig. 5(b). After N&T treatment, almost negligible precipitates were noticed in the weld fusion zone as compared to

PWHT condition. In CGHAZ, both equiaxed laths and PAGBs are noticed, as shown in Fig. 5(c). In PWHT state, less fraction area of precipitates was noticed in CGHAZ as compared to weld fusion zone. The precipitates that dissolve during the welding cycle re-precipitate after the PWHT. The CGHAZ looks similar to the weld fusion zone in N&T condition, as shown in Fig. 5(d). The effect of PWHT and N&T treatment on FGHAZ is shown in Fig. 5(e) and (f), respectively. In PWHT conditions, equiaxed laths, lath boundaries, fine PAGBs, and precipitates along the boundaries are clearly shown in Fig. 5(d). The percentage area of precipitates got reduced in the FGHAZ as compared to that of CGHAZ and weld fusion zone. In FGHAZ, both coarse (remains un-dissolved during welding) and fine precipitates (form during tempering) are noticed. In N&T condition, a similar microstructure is obtained for FGHAZ, CGHAZ, and weld fusion zone except for a negligible amount of precipitates in FGHAZ, as shown in Fig. 5(f). The fraction area of precipitates in the ICHAZ gets reduced as compared to that of weld fusion zone and CGHAZ because of coarsening of existing precipitates but it looks similar to FGHAZ. A complete heterogeneous structure is obtained for the ICHAZ in PWHT conditions.

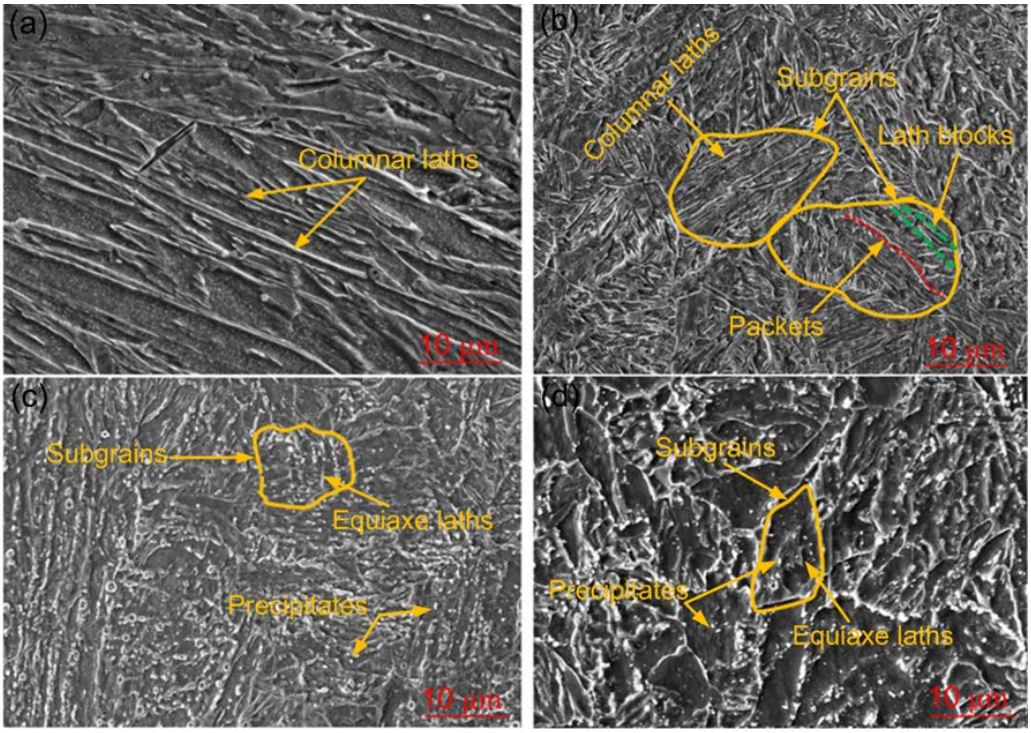

Fig. 4. Secondary electron micrograph of sub-zones for SMAW P92 weldments (a) weld fusion zone, (b) CGHAZ, (c) FGHAZ, and (d) ICHAZ

The PWHT resulted in the coarsening of the un-dissolved existing precipitates which is more than the FGHAZ. The PWHT also resulted in the formation of new precipitates along the grain boundaries and inside the matrix region. Hence, ICHAZ shows both transformed and un-transformed microstructure after the PWHT, as shown in Fig. 5(g). In PWHT state, ICHAZ is characterized by columnar laths, equiaxed laths, existing coarse precipitates, newly developed precipitates, lath boundaries, and sub-grain boundaries. In N&T condition, ICHAZ shows a similar microstructure to other zones of P92 plate weldments. Hence, PWHT resulting the homogenization of microstructure present across the P92 weldments but more effective homogenization of microstructure occurs after the N&T treatment.

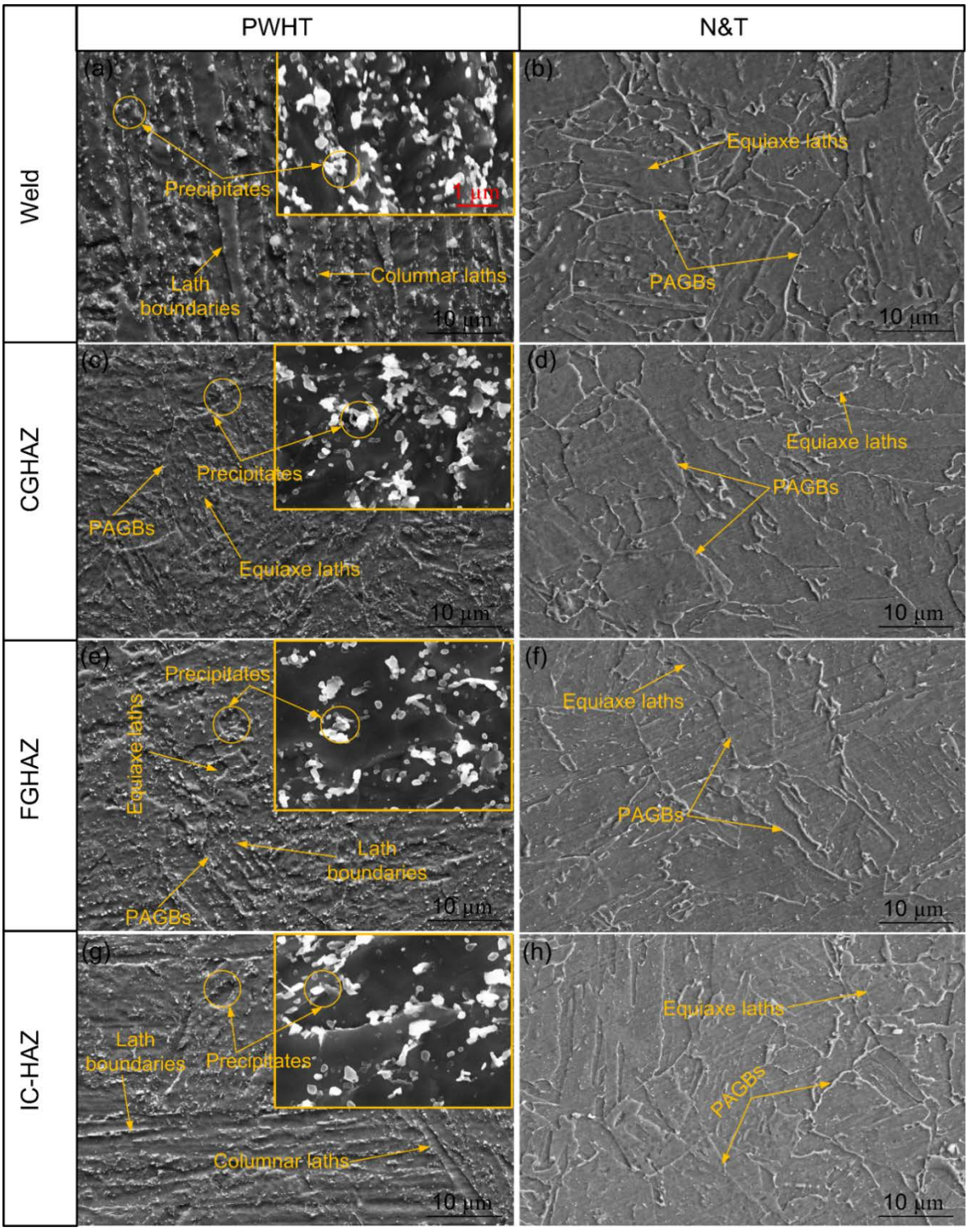

Fig. 5. P92 weldment in PWHT and N&T condition (a), (b) weld fusion zone; (c), (d) CGHAZ; (e), (f) FGHAZ; (g), (h) ICHAZ

Hardness. The hardness of P92 weldments for case I, in different heat treatment conditions are reported in Fig. 6(a-b). In as-welded conditions the complete dissolution of precipitates increases the C and N percentage in the solid solution, resulting in hard lath martensitic structure both in the weld fusion zone and CGHAZ. The hardness measured in the weld fusion zone and CGHAZ are 442 HV and 473 HV, respectively. A considerable change was noticed in hardness value as a move away from the weld fusion line and occurs due to a reduction in C and N content in solid solution. The reduction in C content resulted from the

incomplete dissolution of precipitates in the FGHAZ and ICHAZ. ICHAZ zone is recognized as the soft zone with a minimum hardness value of 214 HV. The lower hardness in FGHAZ and ICHAZ makes it more susceptible to type IV cracking. The hardness measured in the over-tempered base zone was 227 HV which was almost similar to as-received C&F P92 steel. From Fig. 6(a), it is clearly observed that hardness gradient occurred in the P92 weldments in an as-welded condition which renders it weak in-service conditions. The presence of hardness gradient also confirms the variation of microstructure developed across P92 plate weldments. To overcome the hardness gradient across the weldments PWHT and N&T treatment have been carried out. After PWHT, the hardness of the weld fusion zone is reduced from 442 HV to 240 HV and CGHAZ from 473 HV to 247 HV. The hardness of FGHAZ, ICHAZ, and the over-tempered base metal zone was measured 219 HV, 207 HV, and 211 HV. The PWHT reduces the hardness gradient across the P92 weldments but still, a difference in hardness value of weld fusion zone and ICHAZ are noticed. After PWHT, a minute change was noticed in the hardness value of ICHAZ (214 HV to 207 HV). After N&T treatment, the weldment is considered as as-received P92 steel. Hardness variation across the P92 plate weldments in N&T condition is shown in Fig. 6(a). After N&T treatment, hardness measured in deposited metal, CGHAZ, FGHAZ, ICHAZ, and over-tempered base metal were 208 HV, 207 HV, 211 HV, 209 HV, and 215 HV, respectively. The hardness reading confirms that N&T treatment is more effective as compared to that of PWHT to reduce the hardness gradient across the P92 weldments. A negligible hardness variation is noticed across the sub-zone of P92 weldments and weldments can be considered as virgin P92 steel.

Through plate thickness, hardness was also measured, as shown in Fig. 6(b). The variation in weld fusion zone hardness is occurred due to auto-tempering by the subsequent weld passes. A great reduction is noticed in the hardness value of the weld fusion zone after the PWHT. The minimum hardness was measured for the N&T condition.

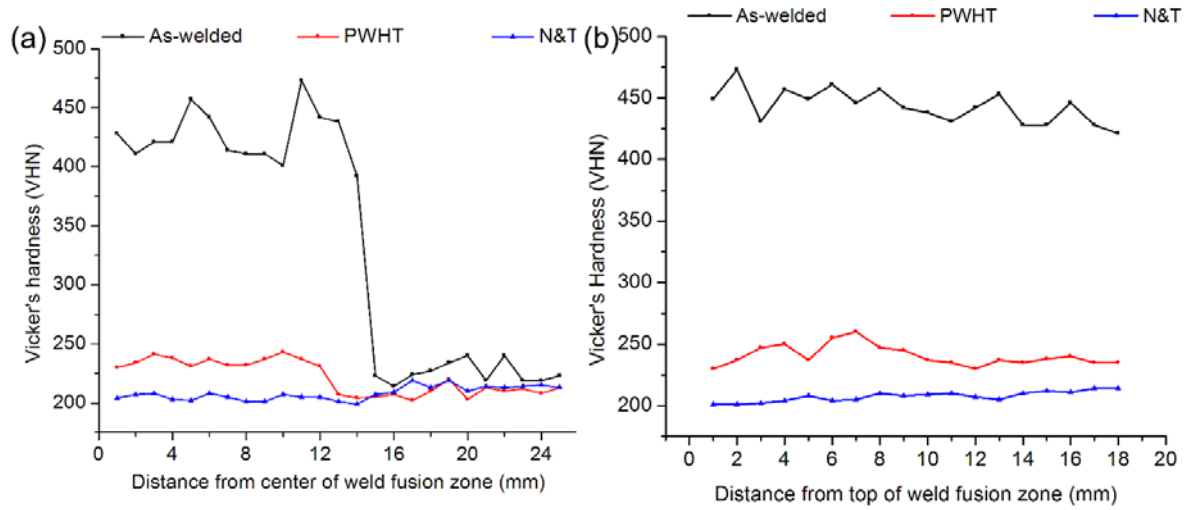

Fig. 6. Hardness variation in different operating conditions (a) in transverse direction and (b) in weld fusion zone along with the thickness

Charpy toughness and fracture surface morphology. The toughness of P92 steel weld is an essential property of weldment evaluated during hydro testing. To avoid brittle fracture during hydro testing of vessels, higher impact toughness of weldment is desired. Pressure vessels are subjected to hydro testing for strength and leaks. To avoid the brittle fracture of P92 steel weldments, a minimum average toughness for weld zone was recommended about 47 J (minimum single value of 38 J) as per EN 1599:1997 and IGCAR-India specification. The results of the Charpy tests are reported in Table 4. In as-welded

condition, Charpy toughness value was obtained lower than the recommended minimum required toughness value of 47 Joules. As the level of diffusible hydrogen increased, the Charpy toughness value was found to be decreased. The maximum value of 16 J was obtained for case I. The hydrogen particles present in the weld fusion zone provide a tri-axial level of stress during the testing. A noticeable change occurs in the Charpy toughness value for each case after the subsequent PWHT and Charpy toughness were obtained more than the minimum desired value. For the first three cases, an almost similar value of Charpy toughness was obtained as shown in Table 4. As the level of hydrogen increased the Charpy toughness value was observed to be decreased and the minimum value was obtained for case IV (56 J). Similar results were obtained for the N&T treatment. The lowest toughness was measured for case IV. The N&T treatment provides a significantly improved toughness value compared to PWHT condition. The PWHT and N&T treatment almost reduce the effect of diffusible hydrogen on Charpy toughness value. The low Charpy toughness value in case III and case IV might be also due to the presence of defects like porosity in the weld fusion zone which cannot be minimized by heat treatment.

Table 4. Charpy test results

Sample No.	As-welded	PWHT	N&T
Case I	16	76	80
Case II	16	72	75
CaseIII	8	70	74
Case IV	7	56	60

In as-welded condition, SEM of the fracture surface of Charpy tested specimen for all the four cases is shown in Fig. 7(a-d). The crack initiation zone is shown at the lower magnification (500x) while the final fracture zone is shown at the top at a magnification of 2000x. In the crack initiation zone, case I show both dimples and quasi-cleavage. The quasi-cleavages are observed besides the ductile dimples, as shown in Fig. 7(a).

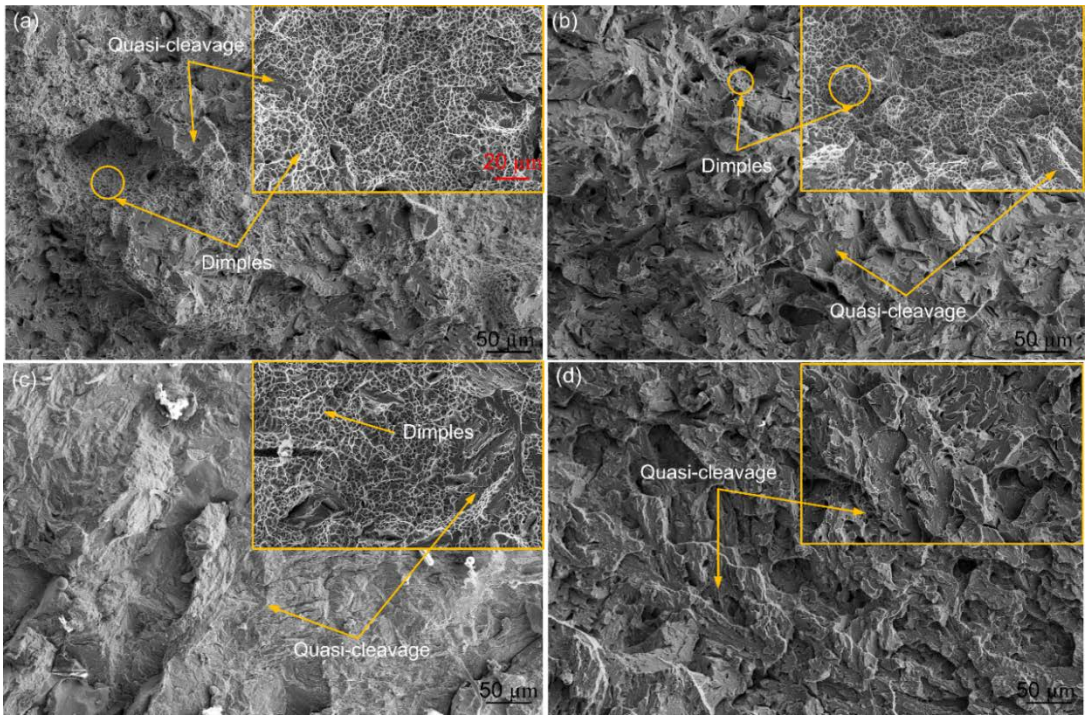

Fig. 7. Fracture surface morphology of impact tested specimen in as-welded condition (a) case I, (b) case II, (c) case III and (d) case IV

For case II, both ductile dimples and quasi-cleavage are noticed in the crack initiation zone but fewer amounts of ductile dimples are noticed compared to quasi-cleavage, as shown in Fig. 7(b). For cases III and IV, the pure quasi-cleavage structure is seen in the crack initiation zone. The final fracture zone of cases I, II, and III are characterized by transgranular ductile tearing, quasi-cleavage, and shear lips. In case I and case II, a negligible amount of quasi-cleavage is noticed in the final fracture zone while for case III, quasi-cleavage is noticed besides the ductile dimples. For case IV, the final fracture zone shows a similar nature as the crack initiation zone. The final fracture zones indicate that the fracture occurred in a completely brittle manner. The smooth inter-crystalline area in case IV shows the embrittling effect. Hence, it can be stated that with an increase in diffusible hydrogen levels in deposited metal, the fracture morphology shifted from the ductile fracture to the brittle fracture.

Effect of heat treatment on fracture surface characteristic of Charpy tested specimen is also carried out, as shown in Fig. 8(a-c).

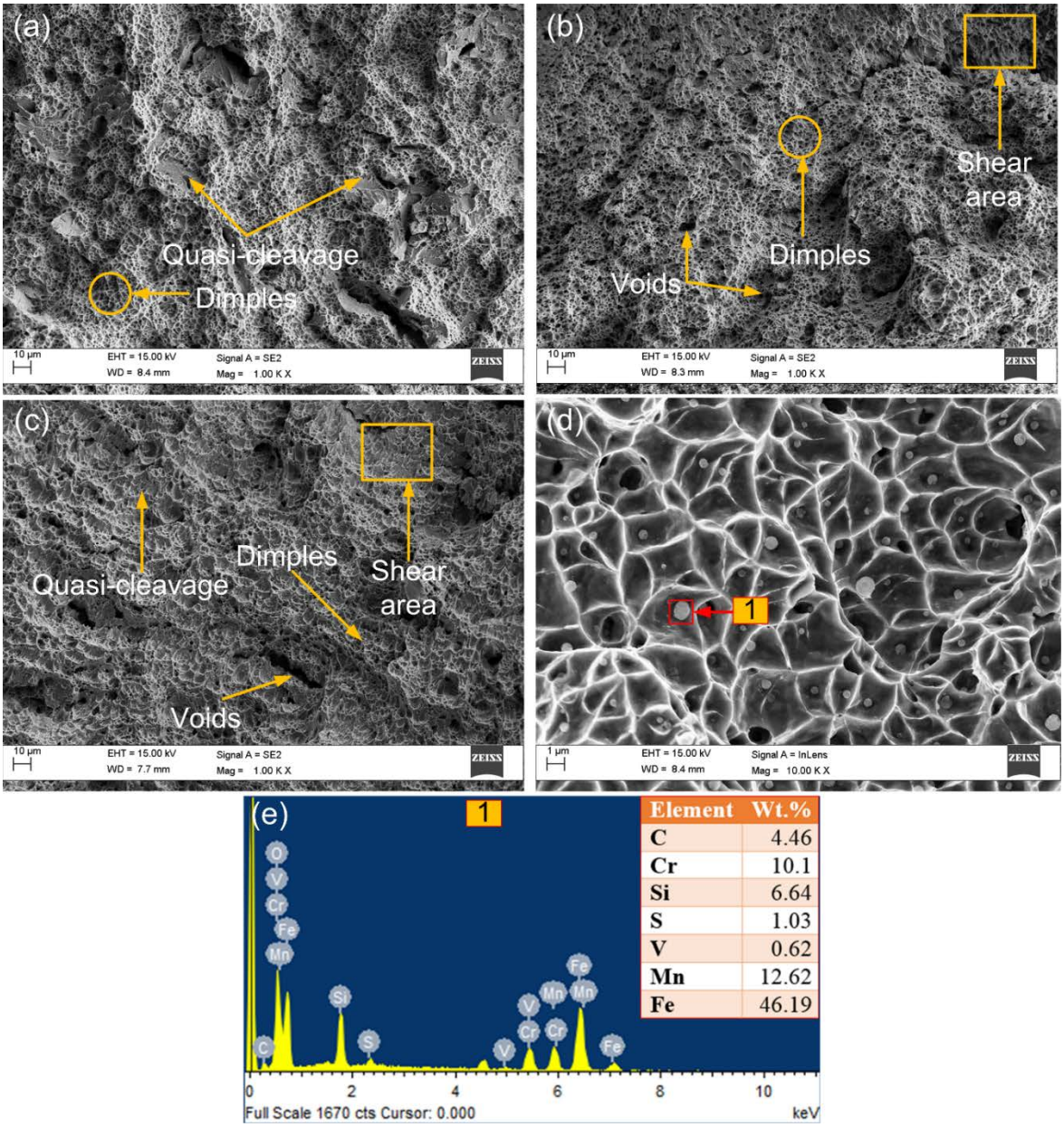

Fig. 8. Secondary electron micrograph of fractured Charpy tested specimen (a) as-welded, (b) PWHT, (c) N&T, (d) as-welded at higher magnification, and (e) the EDS spectra of particles located inside dimples

The fracture surface characteristic in as-welded conditions has been already discussed. In as-welded conditions, large areas of ductile dimples are noticed as compared to quasi-cleavage at the fracture surface. In PWHT conditions, the fracture surface is characterized by dimples, voids, quasi-cleavage, and shear area. Shearing of dimples is clearly noticed in N&T condition, as shown in Fig. 8(b). In N&T condition, a similar pattern of fracture is noticed as in PWHT condition. In N&T condition, shearing of dimples and shear areas are more pronounced as compared to PWHT condition, as shown in Fig. 8(c). In N&T state, the number and size of voids are also increased at the fracture surface as compared to PWHT condition. In the final fracture zone of cases I, II, and III, at higher magnification, the particles are noticed inside the dimples, as shown in Fig. 8(d) (case I). The EDS spectra of the particle are shown in Fig. 8(e), which confirms the presence of Cr, Mn, Fe, V, Si, and S elements. The higher weight percentage of Cr, Fe, Mn, and S indicates the formation of secondary phase particles with MnS at the fracture surface which acts as voids and crack nucleation sites during the testing. The particle size varies from 0.36 to 1.08 μm. The average particle size was measured to be 0.59±0.23 μm.

Tensile test for multi-pass welds joint. The fractured tensile specimen after the ruptured tensile tests is shown in Fig. 9. The gauge diameter for the tensile specimen was 8 mm. In as-welded conditions, the samples were fractured from the gauge area instead of the notch made at the center during tensile tests. The gauge area and reduced area were used for the ultimate tensile strength (UTS) calculation for samples fractured from the gauge area and notch area, respectively. During the tensile tests, a typical fracture phenomenon was observed for some cases. For case IV (as-welded condition), the fracture occurs from the weld fusion zone near the notch area. It might be due to the presence of porosity or embrittling effect. In case I and case II, the fracture occurred from the over tempered base metal (OT-BM) zone instead of the notch area made in the weld. This type of phenomenon was happened due to the higher strength of weld fusion zone as compared to OT-BM which is also confirmed by the hardness results. The microstructure variations across the P92 weldments are responsible for such a type of failure. In case III, the fracture was noticed in the notch area.

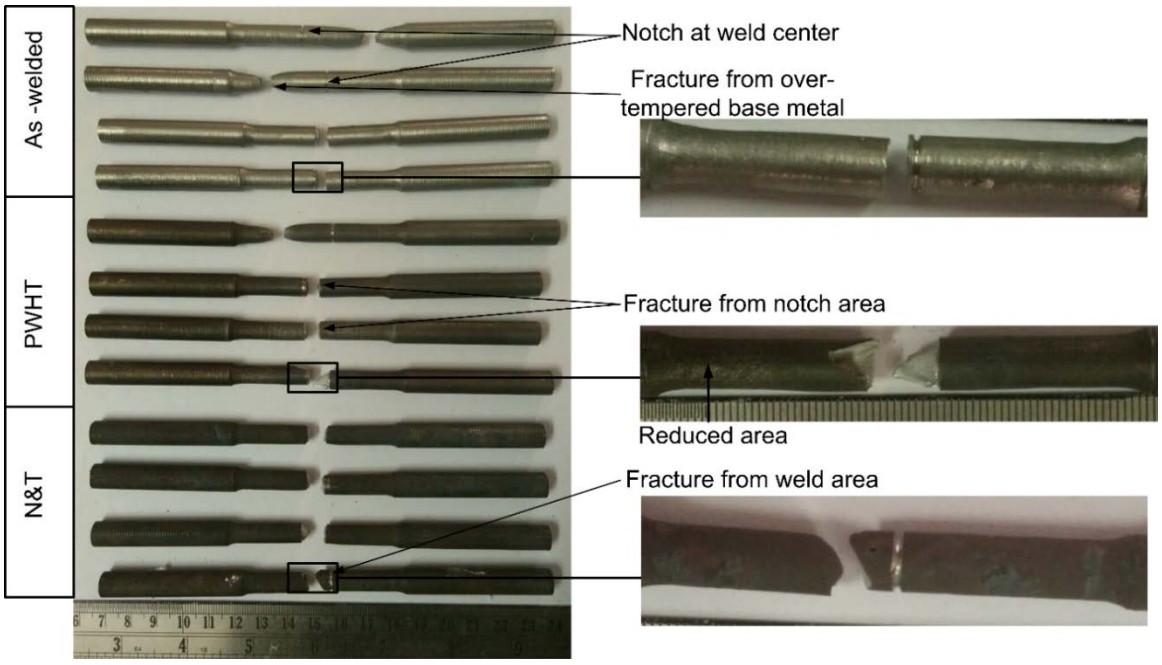

Fig. 9. Ruptured tensile specimens

After PWHT, the microstructure variation and hardness gradient are reduced significantly. However, in case I (PWHT), the weld fusion zone shows a higher strength than the OT-BM, and fractured has occurred from the OT-BM zone. In case IV, the fractured was noticed in the notch area but after fracture, the material is removed up to a large extent, as shown in Fig. 9. The fractured area for case IV is shown at higher magnification. During the tensile testing, the necking formation is started in the OT-BM zone but the final fracture occurs from the notch area. The fractured surface revealed the presence of porosity in the weld fusion zone in the vicinity of the notch area. The porosity is developed due to the presence of a high diffusible hydrogen level in weld consumables.

The N&T treatment provides the homogenized microstructure across the P92 weldments as compared to the PWHT. In the first three cases, fractured occurred from the notch area of the weld fusion zone but case IV again provides different fracture morphology because of the presence of porosity and high hydrogen level. The porosity is clearly noticed at the fractured surface of case IV. In case IV, the fractured occurs from the poor weld fusion zone which is similar to as-welded and PWHT conditions. Hence, an increase in diffusible hydrogen level increases the porosity and embrittling effect in the weld fusion zone which makes it too weak. Hence, the defect and hydrogen level cannot be reduced by any heat treatment process after the completion of the welding.

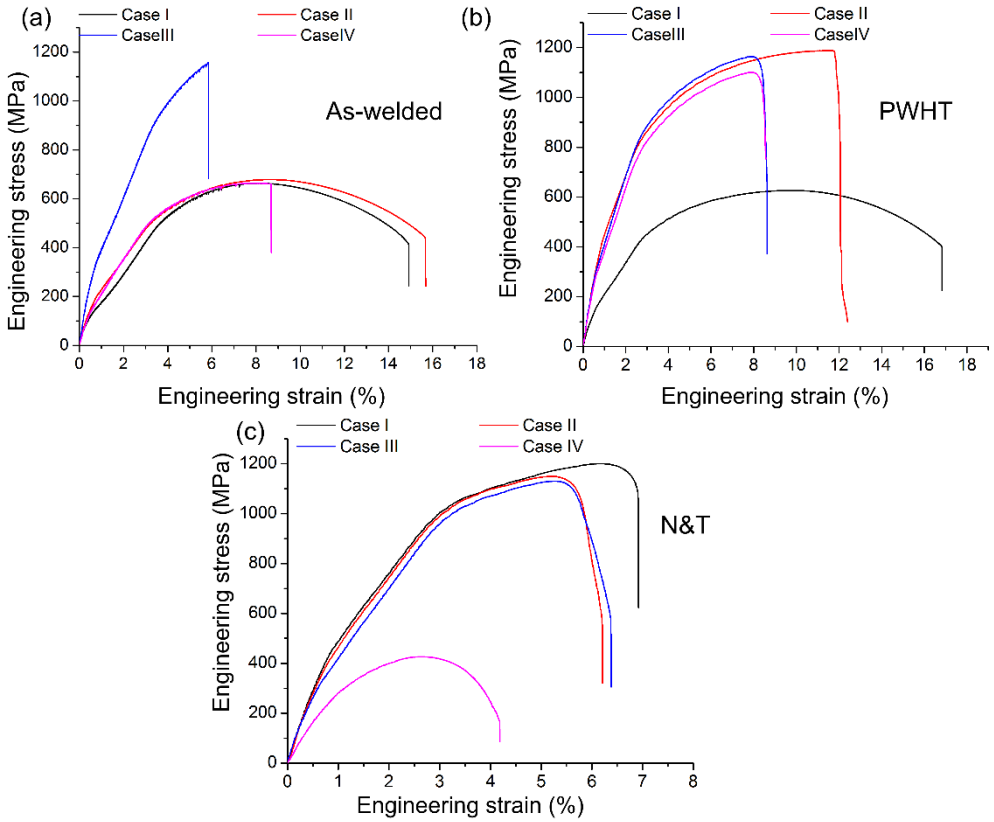

Fig. 10. Engineering stress-strain curve for all the cases in (a) as-welded, (b) PWHT and (c) N&T state

The engineering stress-strain curves for all the cases in different heat treatment conditions are shown in Fig.10. The tensile test results are depicted in Table 5. In case I and case II (as-welded) low UTS we obtained due to fracture from the OT-BM zone. They produced the strength of OT-BM which is almost similar to the UTS of as-received C&F P92 steel (655.5 MPa). In case III, higher UTS was obtained for the weld fusion zone. In case IV, the results obtained for the weld fusion zone were too poor as compared to case III because of

the presence of higher porosity and diffusible hydrogen level. The fracture occurs near the notch made in the weld fusion zone.

Table 5. Tensile test results

Case No.	As-welded			PWHT			N&T		
	UTS (MPa)	YS (MPa)	Fracture location	UTS (MPa)	YS (MPa)	Fracture location	UTS (MPa)	YS (MPa)	Fracture location
Case I	663	535	OT-BM	627	470	OT-BM	1201	955	Notch made in weld
CaseII	679	550	OT-BM	1188	910	Notch made in weld	1150	900	Notch made in weld
Case III	1156	1020	Notch made in weld	1164	890	Notch made in weld	1130	880	Notch made in weld
Case IV	664	618	Weld zone	1101	720	Notch made in weld	427	350	Weld zone

After the PWHT, a uniform structure formation is noticed. In case I, the strength gradient is not removed completely and fracture occurs from the OT-BM zone instead of the weld fusion zone. The UTS obtained in case I was lower than the as-received material because of tempering. In the last three cases, the fractures occurred from the notch area made in the center of the weld fusion zone. For cases II, III, and IV, the fracture was occurred in a brittle manner, as shown in Fig. 10(b). An increase in diffusible hydrogen level in the weld consumable also reduces the UTS after the PWHT. In case IV, the lower UTS was measured.

After N&T treatment, for cases I, II, and III, fractured were noticed in the notch area and provided the UTS of the weld fusion zone. In case I, higher UTS was obtained about 1201 MPa. The UTS gets reduced with an increase in the level of hydrogen in the weld fusion zone. In case IV, fracture occurred from the weld fusion zone in the vicinity of the notch area. This resulted due to the presence of a defect in the weld fusion zone and a high level of diffusible hydrogen. The lower UTS were reported for case IV, which was also less than the minimum required value. The fractured was occurred in a brittle manner without any prior notice for all cases of N&T treatment, as shown in Fig. 10(c). Hence, N & Thomogenizes the microstructure and remove the strength gradient but the effect of diffusible hydrogen level cannot be minimized.

Flexural test for multi-pass welds joint. For both top and root bend tests, specimens with dimensions 160mm×12.5mm×10mm were machined from the welded plate. The schematic of the flexural test specimen is shown in Fig. 11(a). The bend radius of the three-point bend roller was 10 mm. In all bending tests, each data point represented an average of two specimens. The fracture flexural test specimens were analyzed by using the FESEM. Three-point bending tests were performed at room temperature for both the top and root sides. The fractured three-point top bend test specimens are shown in Fig. 11(b). The results of the flexural tests are depicted in Table 6.

In as-welded conditions, the weld fusion zone consisted of the brittle martensitic structure. In case I, the fracture occurred from the weld fusion zone, as shown in Fig. 11(b). In case II, the bending angle reaches up to 180^{o} with a crack along the weld fusion boundary or CGHAZ. In cases III and IV, porosity is clearly seen in the weld fusion zone. Porosity present in the fusion zone acts as the stress concentrator during the flexural test and failure mainly

occurs due to the crack initiated from the porosity. In cases III and IV, the fracture was noticed in the fusion zone. The complete brittle fracture was noticed in case III and case IV. In cases I, III, and IV, the fracture was noticed in the weld fusion zone while in case II, the fracture was noticed in the fusion line. Guo et al. [38] had also reported the fracture of the welded joint in the fusion zone during the three-point bending test on the top side. Li et al. [39] had also reported the failure of the welded joint from the fusion zone during the three-point bending test of the top side. The microcracks would be subjected to compressive stress during the top bending test and will not propagate easily.

Table 6. Top and root bend test results

Specimen	Top side			Root side		
	Flexural strength (MPa)	% elongation	Load (kN)	Flexural strength (MPa)	% elongation	Load (kN)
Case I	1621	25.62	13.78	1702	22.53	14.47
Case II	1616	23.38	13.6	1642	27.52	13.97
Case III	1524	13.45	13.06	1393	4.55	12.09
Case IV	1445	5.1	12.85	1234	2.9	10.49

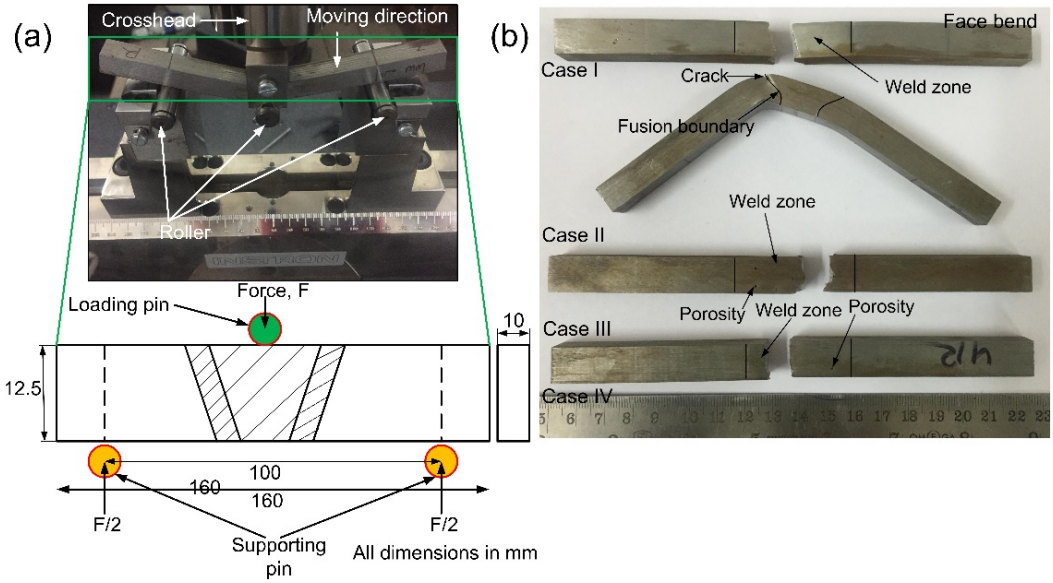

Fig. 11. (a) Schematic of flexural test and (b) three-point bending test specimens for top side

The flexural strength measured for case I, case II, case III, and case IV were 1621 MPa, 1616 MPa, 1524 MPa, and 1424 MPa. The flexural strength was found to be decreased with a change in electrode condition from case I to case IV. The main reason for the decrement was the presence of diffusible hydrogen in the weld fusion zone for case III and case IV. The electrode used in backed condition and as-supplied condition were provided similar results. The weld fusion zone has a martensitic structure for each case but a change in electrode condition introduces the porosity and some other type of defects in the weld fusion zone. The engineering stress-strain curve for three-point top bending of multi-pass butt welded joint is shown in Fig. 12(a). From Fig. 12(a), the fracture noticed in cases III and IV was brittle mode while for case I and case II, yielding has been noticed. In cases II and III, a sudden dip in the curve (highlighted in green circle) was noticed. The sudden dip in the flexural curve shows the presence of porosity of a smaller size from which cracks were initiated but not converted into the final fracture. In case I, no sudden dip was noticed and it indicates the porosity-free weld fusion zone for case I. The % elongation measured for the case I and IV were 25.62 and

5.1%. Hence, the presence of porosity in the weld fusion zone affects the ductility of material to a great extent. As the level of hydrogen increased in the electrode, the % elongation was found to be decreased for top bending tests.

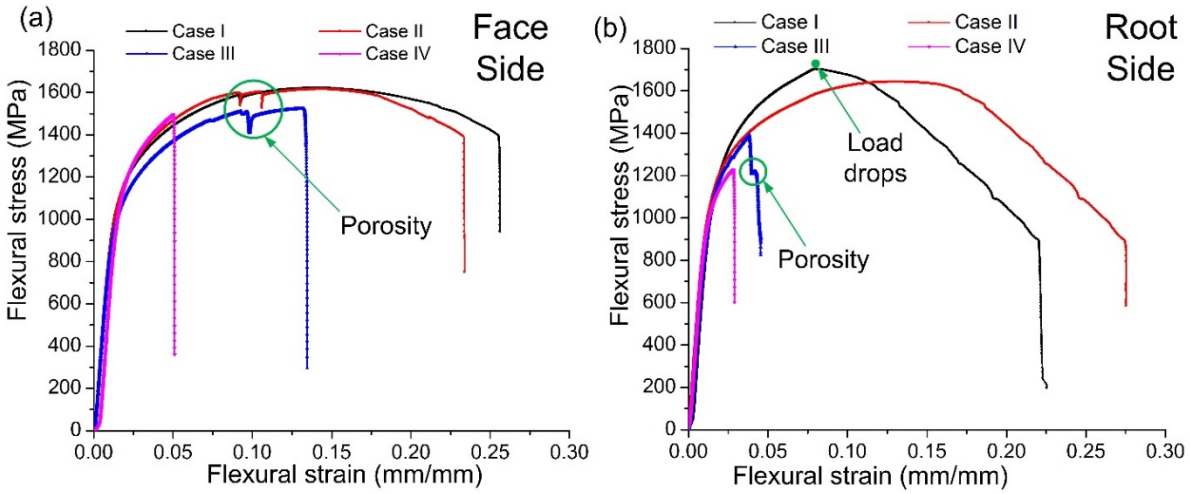

Fig. 12. Three-point bending test results performed at room temperature for multi-pass welded joint of P92 steel (a) top side and (b) root side

Three-point root bend test specimens are shown in Fig. 13. Three-point root bending test plot for the different conditions of the electrode is shown in Fig. 12(b). Maximum flexural strength was noticed about 1702 MPa for case I. For cases I and II, the fracture occurred with yielding but in cases III and IV, no yielding was noticed. The sudden fracture for case III and case IV looks similar to top bend test and provides the brittle mode of fracture. In case I and case II, the complete yielding occurred without any crack. The flexural strength measured for case IV was 1234 MPa which was much less than case I. The ductility measured for cases III and IV were 4.55 and 2.9% which were also much less than case I and case II. The fluctuation in the curve was noticed due to the presence of minute porosity in the weld fusion zone. For root bend tests, the fracture has been reported in the fusion line by Guo et al. [38].

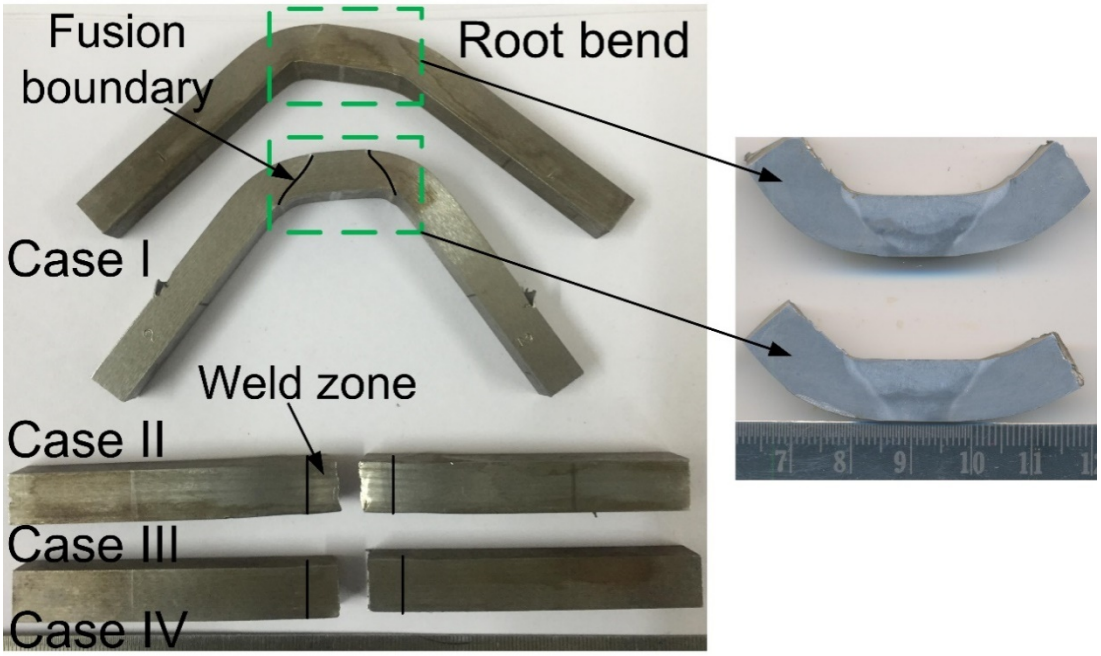

Fig. 13. Three-point bending test specimens for root side

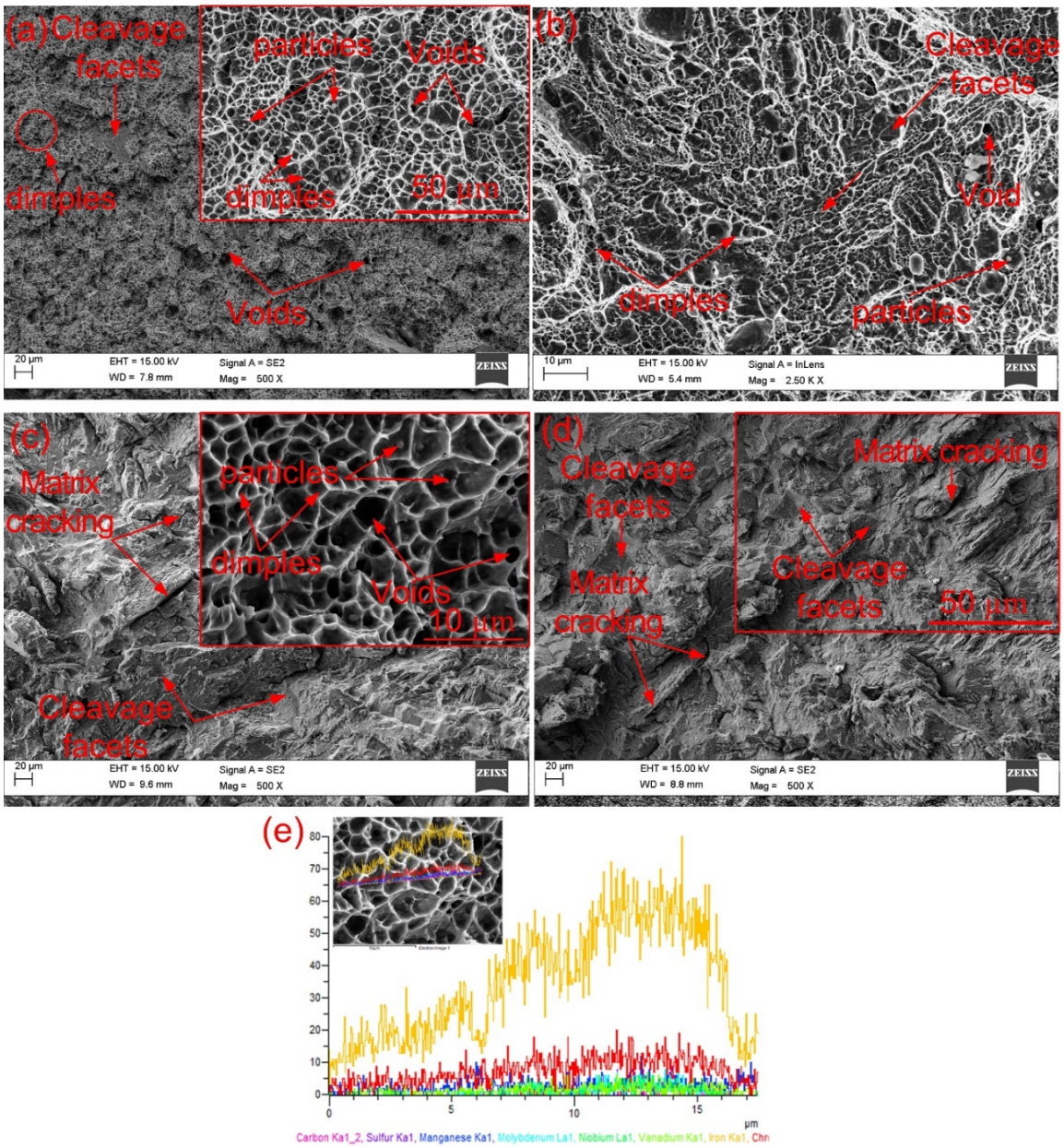

Fig. 14. Secondary electron micrograph of fractured three-point bend test specimens for top side (a) case I, (b) case II, (c) case III, (d) case IV, and (e) EDS line scan of the fracture surface

Flexural test for multi-pass welds joint. The secondary electron fractography of the flexural test specimen is shown in Fig. 14(a-d). In case I, the fracture surface of the crack initiation zone revealed the ductile dimples and fewer amount of cleavage facets. Small size voids were also noticed in the crack initiation zone, as shown in Fig. 14(a). The final fracture zone is shown in the top right of Fig. 14(a). The final fracture surface revealed the ductile mode of fracture and both voids and dimples were seen on the fractography. In the final fracture zone, small size particle was distributed uniformly inside the ductile dimples. In case II, the final fracture zone showed the mixed mode of fracture. Cleavage facets and ductile dimples both were noticed on the fracture surface. In case II, the number of voids was found to increase as compared to case I. In case III, the crack initiation zone was characterized by cleavage facets with a negligible amount of dimples. The matrix cracking is clearly seen in the crack initiation zone, as shown in Fig. 14(c). The final fracture zone is characterized by

dimples with voids of bigger size as compared to case I and case II. In case IV, an interesting pattern of fracture was observed. The crack initiation zone and final fracture zone were characterized by cleavage facets and matrix cracking. The EDS line scan of the fracture surface was also carried out for case I. The EDS line scan confirmed the presence of Cr, Fe Mo, and Mn containing precipitates. In the line-scan presence of S and Mn confirmed the manganese sulfide (MnS) particles at the fracture surfaces. The presence of MnS particles inside the dimples is also seen in the final fracture zone of Fig. 14(a-c).

The MnS particles may act as the crack nucleation sites because of brittleness. The Cr-rich $M_{23}C_6$ and V and Nb-rich MX particles may also act as the stress concentrator. The segregation of S along the crack tip has also been reported by Hippsley [40]. In plain 9Cr-1Mo steel, wedge crack formation due to lath boundaries splitting had also been reported by Choudhary et al. [41]. The presence of silicon and phosphorous in P92 steel promoted the splitting of lath boundaries. A higher percentage of phosphorous in P91 steel makes it susceptible to phosphorous embrittlement [42].

4. Conclusions

1. The P92 steel weld joint was performed four different levels of weld constables provided a different level of diffusible hydrogen.
2. The P92 steel weld joints were subjected to top and root flexural bend tests. The axial and transverse residual stresses were also measured experimentally in different welded plates using the blind hole drilling method.
3. The residual stresses were matched fairly with numerically obtained results for case I low level of diffusible hydrogen.
4. The axial and transverse shrinkage stresses were measured at different locations, the centre of the weld fusion zone and HAZ.
5. The maximum magnitude of residual stresses was measured at the centre of the weld fusion zone. The maximum value of transverse stresses was measured to be 355 MPa for case IV.
6. The numerical analysis of residual shows unsymmetrical distributions in the weld fusion zone. The predicted residual stress value match fairly well with numerically obtained residual stress at the outer surfaces and at the root section.

References

[1] Mahapatra MM, Datta GL, Pradhan B, Mandal NR. Modelling the effects of constraints and single axis welding process parameters on angular distortions in one-sided fillet welds. *Proc. IMechE Part B J. Eng. Manuf.* 2006;221(3): 397-407.
[2] Cottam R, Luzin V, Thorogood K, Wong YC, Brandt M. The role of metallurgical solid state phase transformations on the formation of residual stress in laser cladding and heating. *Mater. Sci. Forum.* 2014;777: 19-24.
[3] De A, Debroy T. A perspective on residual stresses in welding. *Sci. Technol. Weld. Join.* 2017;16(3): 204-208.
[4] Biswas P, Mandal NR, Vasu P, Padasalag SB. Analysis of welding distortion due to narrow-gap welding of upper port plug. *Fusion Eng. Des.* 2010;85(5): 780-788.
[5] Biswas P, Mandal NR, Das S. Prediction of welding deformations of large stiffened panels using average plastic strain method. *Sci. Technol. Weld. Join.* 2011;16(3): 227-231.
[6] Ghosh PK, Kumar RR, Devakumaran K. Effect of pulse current on shrinkage stress and distortion in multi pass GMA welds of different groove sizes. *Indian Weld. J.* 2010;87: 43-53.
[7] Basavaraju C. Simplified analysis of shrinkage in pipe to pipe butt welds. *Nucl. Eng. Des.* 2000;197(3): 239-247.
[8] Webster GA, Eeilo AN. Residual stress distributions and their influence on fatigue lifetimes. *Int. J. Fatigue.* 2001;23(1): 375-383.

[9] Dong P, Dong P. Residual stresses and distortions in welded structures : a perspective for engineering applications Residual stresses and distortions in welded structures : a perspective for engineering applications. *Sci. Technol. Weld. Join.* 2004;10(4): 389-398.
[10] Kumar PG, Yu-ichi K. Diffusible hydrogen in steel weldments. *Trans. JWRI.* 2013;42: 39-62.
[11] Yaghi AH, Hyde TH, Becker AA, Sun W. Finite element simulation of welding and residual stresses in a P91 steel pipe incorporating solid-state phase transformation and post-weld heat treatment. *IMechE J. Strain Anal.* 2008;43(5): 275-293.
[12] Dong P. Residual Stress Analyses of a Multi-Pass Girth Weld: 3-D Special Shell Versus Axisymmetric Models. *J. Press. Vessel Technol.* 2001;123(2): 207-213.
[13] Zubairuddin M, Albert SK, Vasudevan M, Mahadevan S, Chaudhri V, Suri VK. Thermomechanical analysis of preheat effect on grade P91 steel during GTA welding. *Mater. Manuf. Process.* 2016;31(3): 366-371.
[14] Dean D, Hidekazu M. Prediction of welding residual stress in multi-pass butt-welded modified 9Cr–1Mo steel pipe considering phase transformation effect. *Comput. Mater. Sci.* 2006;37(3): 209-219.
[15] Murakawa H, Miloslav B, Adan V, Sherif R, Cartin MD, David D, Kamran MN. Effect of phase transformation onset temperature on residual stress in welded thin steel plates. *Trans. JWRI.* 2008;37(2): 75-80.
[16] Loöpez-Ramirez S, Barreto JDJ, Palafox-Ramos J, Morales RD, Zacharias D. Modeling study of the influence of turbulence inhibitors on the molten steel flow, tracer dispersion, and inclusion trajectories in tundishes. *Metall. Mater. Trans. B.* 2001;32: 615-627.
[17] Cabrera-Marrero JM, Carreno-Galindo V, Morales RD, Chavez-Alcala F. Macro-Micro modeling of the dentritic microstructure of steel billets processes by continuous casting. *ISIJ Int.* 1998;38(8): 812-821.
[18] Mitra A, Siva Prasad N, Janaki Ram GD. Estimation of residual stresses in an 800 mm thick steel submerged arc weldment. *J. Mater. Process. Technol.* 2016;229: 181-190.
[19] Mitra A, Siva Prasad N, Janaki Ram GD. Influence of temperature and time of post-weld heat treatment on stress relief in an 800-mm-thick steel weldment. *J. Mater. Eng. Perform.* 2016;25: 1384-1393.
[20] Deng D, Murakawa H, Liang W. Numerical and experimental investigations on welding residual stress in multi-pass butt-welded austenitic stainless steel pipe. *Comput. Mater. Sci.* 2008;42(2): 234-244.
[21] Sattari-Far Y, Javadi I. Influence of welding sequence on welding distortions in pipes. *Int. J. Press. Vessel. Pip.* 2008;85(4): 265-274.
[22] Kim S, Kim J, Lee W. Numerical prediction and neutron diffraction measurement of the residual stresses for a modified 9Cr – 1Mo steel weld. *J. Mater. Process. Technol.* 2009;209(8): 3905-3913.
[23] Ghosh PK, Kumar RR, Pramanick AK. Effect of pulse current on shrinkage stress and distortion in multi pass GMA welds of different groove sizes. *Indian Weld. JournalWelding J.* 2010;43-s: 14-24.
[24] Anant R, Ghosh PK. Experimental investigation on transverse shrinkage stress and distortion of extra narrow and conventional gap dissimilar butt joint of austenitic stainless steel to low alloy steel. In: *Proc. Int. Conf. Mining, Mater. Metall. Eng.* 2014. p.1-5.
[25] Arunkumar S, Rangarajan P, Devakumaran K, Sathiya P. Comparative study on transverse shrinkage, mechanical and metallurgical properties of AA2219 aluminium weld joints prepared by gas tungsten arc and gas metal arc welding processes. *Def. Technol.* 2015;11(3): 262-268.

[26] Yaghi AH, Hyde TH, Becker AA, Sun W, Hilson G, Simandjuntak S, Flewitt PEJ, Smith DJ. A comparison between measured and modeled residual stresses in a circumferentially butt-welded P91 steel pipe. *J. Press. Vessel Technol.* 2010;132(1): 1-10.
[27] Paddea S, Francis JA, Paradowska AM, Bouchard PJ, Shibli IA. Residual stress distributions in a P91 steel-pipe girth weld before and after post weld heat treatment. *Mater. Sci. Eng. A.* 2012;534: 663-672.
[28] Venkata KA, Kumar S, Dey HC, Smith DJ, Bouchard PJ. Study on the effect of post weld heat treatment parameters on the relaxation of welding residual stresses in electron beam welded P91 steel plates. *Procedia Eng.* 2014;86: 223-233.
[29] Chuvas TC, Garcia PSP, Pardal JM, Fonseca M da PC. Influence of heat treatment in residual stresses generated in P91 steel-pipe weld. *Mater. Res.* 2015;18(3): 614-621.
[30] Kulkarni S, Ghosh PK, Ray S. Improvement of weld characteristics by variation in welding processes and parameters in joining of thick wall 304LN stainless steel pipe. *ISIJ Int.* 2008;48(11): 1560-1569.
[31] Zhao Y, Gong J, Wang Y, Wei G. Effect of start/stop position distribution on residual stresses in the multi-pass welded 12Cr1MoV/P91 dissimilar pipe. *Int. J. Steel Struct.* 2014;14: 539-546.
[32] Hempel N, Nitschke-pagel T, Dilger K. Residual stresses in multi-pass butt-welded ferritic-pearlitic steel pipes. *Weld World.* 2015;59: 555-563.
[33] Satyarthi MK, Pandey PM. Modeling of material removal rate in electric discharge grinding process. *Int. J. Mach. Tools Manuf.* 2013;74: 65-73.
[34] Sharma V, Pandey PM. Optimization of machining and vibration parameters for residual stresses minimization in ultrasonic assisted turning of 4340 hardened steel. *Ultrasonics.* 2016;70: 172-182.
[35] Mulik RS, Pandey PM. Magnetic abrasive finishing of hardened AISI 52100 steel. *Int. J. Adv. Manuf. Technol.* 2011;55: 501-515.
[36] Panait CG, Bendick W, Fuchsmann A, Gourgues-Lorenzon AF, Besson J. Study of the microstructure of the Grade 91 steel after more than 100,000 h of creep exposure at 600 °C. *Int. J. Press. Vessel. Pip.* 2010;87(6): 326-335.
[37] Holdstock R. *Inducing hydrogen assisted cold cracking in high strength steel weld metal. Ph.D. Thesis*. 2016.
[38] Guo N, Yang Z, Wang M, Yuan X, Feng J. Microstructure and mechanical properties of an underwater wet welded dissimilar ferritic/austenitic steel joint. *Strength Mater.* 2015;47: 12-18.
[39] Li HL, Liu D, Yan YT, Guo N, Feng JC. Microstructural characteristics and mechanical properties of underwater wet flux-cored wire welded 316L stainless steel joints. *J. Mater. Process. Technol.* 2016;238: 423-430.
[40] Feng CA. Sulphur segregation and high-temperature brittle intergranular fracture in alloy steels. *Acta Metall.* 1987;35(10): 2399-2416.
[41] Choudhary BK, Isaac Samuel E. Creep behaviour of modified 9Cr-1Mo ferritic steel. *J. Nucl. Mater.* 2011;412(1): 82-89.
[42] Sathyanarayanan S, Moitra A, Samuel KG, Sasikala G, Ray SK, Singh V. Evaluation of dynamic fracture toughness based reference temperature (Tody) of modified 9Cr-1Mo steel in phosphorus embrittled and cold-worked condition. *Mater. Sci. Eng. A.* 2008;488(1-2): 519-528.

THE AUTHORS

Pal Vinay Kumar
e-mail: gaurishankar.vinaypal@gmail.com
ORCID: 0000-0001-7830-570X

Singh L.P.
e-mail: lpsingh1976@gmail.com
ORCID: 0000-0002-6221-8174